Materials Today Chemistry 47 (2025) 102835

Contents lists available at ScienceDirect

Materials Today Chemistry

journal homepage: www.journals.elsevier.com/materials-today-chemistry/

Transferrin-stabilized bimetallic nanoclusters: Design of a new fluorescent biosensor to identify tryptophan metabolites

Árpád Turcsányi [a,b], Ádám Juhász [a,b], Edit Csapó [a,b,*]

[a] MTA-SZTE Lendület „Momentum" Noble Metal Nanostructures Research Group, University of Szeged, Rerrich B. sq. 1, Szeged, H-6720, Hungary
[b] Interdisciplinary Excellence Center, Department of Physical Chemistry and Materials Science, University of Szeged, Rerrich B. sq. 1, Szeged, H-6720, Hungary

ARTICLE INFO

Keywords:
Iron-binding protein
Gold-silver nanocluster
Fluorescence enhancement
Detection
3-Hydroxyanthranilic acid

ABSTRACT

The determination of neuroactive molecules is an important task in the monitoring of patient health. In this work, a one-step, green preparation protocol has been newly developed to synthesize highly reddish-orange-emitting gold-silver bimetallic nanoclusters reduced and stabilized by transferrin protein (Tf-AuAg NCs). The fabrication route of these bimetallic NCs was optimized first based on different parameters (gold:silver ratio, transferrin and metal concentrations, temperature and synthesis time). The properties of the nanoclusters (NCs) having a controlled gold/silver ratio were thoroughly analyzed using multiple methods, focusing on their optical characteristics. The source and various characteristics (excitation, emission maximum, lifetime) of the emitting species were also determined. Additional quenching studies were performed using iodide, a well-known quencher of tryptophan, to check the effect on different emission peaks. This newly fabricated NCs can play an important role as a sensing agent. Thus, sensing measurements were conducted on tryptophan metabolites (kynurenine and serotonin pathway, a total of 15 molecules) in three different media (phosphate buffered saline (PBS), artificial cerebrospinal fluid (aCSF) and diluted human serum), determining the limit of detection for 3-hydroxyanthranilic acid at 0.55 and 0.32 μM in PBS and aCSF. This molecule is a fluorophore itself whose detection is problematic due to many interfering substances (for example anthranilic acid), while its selective enhancement distinct from other kynurenine pathway molecules can be used for determination at the NCs emission wavelength centered around 610 nm. Additional calorimetric studies were also performed to identify the interaction between the sensed molecule and the Tf-AuAg NCs.

1. Introduction

Nanoclusters (NCs) are very small particles, usually built of several or few hundred atoms. These formulations possess unique characteristics different from the atoms or conventional nanoparticles [1]. In the case of noble metal NCs, they lack the well-known plasmonic property (collective oscillation of electrons at certain energy levels) of the nanoparticles (NPs) due to their minuscule size, as well as the distinctive color connected to the plasmon frequency of the NPs. This sub-nanometer size also causes the electron levels to be separated compared to the NPs or the metallic bulk phase, which means that no valence or conducting band is present in the NCs. Instead, molecule-like properties arise in these particles, such as fluorescence, magnetic properties or chirality. These new characteristics can be efficiently utilized in many fields, e.g. labeling, bioimaging, sensing and catalysis [2–5]. Furthermore, the incorporation of a second metal into the NCs can enhance and tune their properties which can be used to broaden their field of application [6].

The preparation of NCs is heavily concentrated on the formation and stabilization of very small-sized particles, so the inhibition of particle growth is very important [7]. This is achieved by using reducing agents which create many particle cores and stabilizing agents which effectively limit particle growth and aggregation, resulting in the formation of few nm sized NCs instead of the 10−100 nm NPs. When proteins are used as stabilizing agents, multiple advantages can be exploited. First, they can be applied as reducing agents because their tyrosine (Tyr) building blocks can reduce the metal ions at very high pH [8,9]. Second, their inherent specific drug-binding properties make them ideal ligands for subsequent applications such as sensing, targeted delivery and fluorescent labeling [10–12]. In addition, their intrinsic functions may

* Corresponding author. MTA-SZTE Lendület „Momentum" Noble Metal Nanostructures Research Group, University of Szeged, Rerrich B. sq. 1, Szeged, H-6720, Hungary.
E-mail addresses: tarpad@chem.u-szeged.hu (Á. Turcsányi), juhaszne@chem.u-szeged.hu (E. Csapó).

https://doi.org/10.1016/j.mtchem.2025.102835
Received 21 February 2025; Received in revised form 23 May 2025; Accepted 20 June 2025
Available online 23 June 2025

be retained even after NC synthesis creating multifunctional materials [13]. Furthermore, the protein makes the formulations biocompatible and biodegradable, which is a must for *in vivo* usage in medical and pharmaceutical applications.

Fluorescent NCs can be efficiently utilized in sensing applications, as their stabilizing ligands make it possible to bind specific molecules, affecting their optical properties. Most publications describe sensing based on quenching of the fluorescence, where the binding molecule usually opens a pathway for non-radiative decay, thereby reducing the chance of the emission of a fluorescent photon [14–16]. In other cases, the binding of the sensed molecule causes a rise in fluorescence through a controlled aggregation, which makes the ligands more rigid, reducing the chance of non-radiative energy transfer, thus increasing the fluorescence. This phenomenon is usually cited as aggregation induced emission enhancement (AIE for short), which happens for fluorescent dyes and NCs as well [17,18].

Kynurenine pathway molecules all have distinct effects on the human body. These molecules are all metabolites of tryptophan, and they can modify neurotransmission and immune response. Anthranilic acid (AA) is associated with the suppression of the expression or activation of the transforming growth factor β [19]. Kynurenic acid (Kyna) promotes the kynurenase A reaction (turning L-kynurenine (Kyn) into AA), thus decreasing the 3-hydroxyanthranilic acid (3-HAA)/anthranilic acid ratio. This molecule can also take part in anti-inflammatory processes, and the regulation of its concentration in tissues can be an effective tool in many treatments. 2-picolinic acid (PA) has antiproliferative and neuroprotective properties, similarly to Kyna [20]. Other intermediates of the pathway are, however, neurotoxic (3-hydroxy-DL-kynurenine (HKyn) and quinolinic acid (QA) with its excitotoxic property). The changes in their concentration can be an indicator of several neurological diseases (schizophrenia, Alzheimer's, Parkinson's and Huntington's disease); therefore the effective monitoring of their apparent concentration is a very important, albeit a challenging task [21–23]. While tryptophan is majorly metabolized through the kynurenine pathway (~85 %), around 1 % is converted into serotonin (5-hydroxytriptamine, HTA) and its related compounds. Serotonin also takes part in important biological processes as a neurotransmitter and the changes in its level in the body can cause multiple disorders [17].

The aim of this work was to prepare novel transferrin-stabilized bimetallic gold-silver nanoclusters (Tf-AuAg NCs) and optimize their optical and colloidal parameters through varying their synthesis conditions. In the literature, there are some publications on monometallic systems (Tf-Au NCs) [17,24], but no data on bimetallic derivatives. The optical properties are strongly modified by the incorporation of a new metal; thus, there is a continuous demand for the development of new bimetallic NCs. Successful preparation of Tf-AuAg NCs was followed by thorough characterization focusing mainly on their photoluminescence. Developing new NCs for the detection of tryptophan metabolites (for example L-kynurenine [25] and kynurenic acid [26]) is a major goal of our research group. Continuing this work, the NCs were employed in the fluorescent sensing of neuroactive molecules from the kynurenine and serotonin pathways in three different matrices, namely phosphate buffered saline (PBS), artificial cerebrospinal fluid (aCSF) and in human serum. In the case of 3-hydroxyanthranilic acid, a more thorough investigation was executed to determine the limit of detection and to explore the reaction through calorimetric studies.

2. Materials and methods

2.1. Materials

For the synthesis of NCs, human apo-transferrin (M_r = 79570 Da, BioReagent, 98 %, agarose gel electrophoresis, suitable for cell culture) was supported by Sigma Aldrich, hydrogen tetrachloroaurate ($HAuCl_4 \times 3H_2O$, 99.9 %, Au content 49 %) was from Alfa Aesar, silver nitrate ($AgNO_3$, a.r. grade, 99.9 %) and sodium hydroxide (NaOH, 98 %) were from Molar Chemicals. For ionic strength and pH-dependence studies, sodium chloride (NaCl, 99 %) was also from Molar Chemicals and hydrochloric acid (37 % solution) was obtained from VWR. For the preparation of PBS (pH = 7.4, 0.9 w% NaCl content), sodium dihydrogen monophosphate ($NaH_2PO_4 \times 2H_2O$, 99 %), disodium hydrogen monophosphate ($Na_2HPO_4 \times 12H_2O$, 99 %) were from Molar Chemicals. For quenching studies, potassium iodide (KI, puriss) was used from Molar Chemicals. The aCSF medium was prepared using potassium dihydrogen monophosphate (KH_2PO_4, a.r.) from Reanal, sodium bicarbonate ($NaHCO_3$, 99.5 %) from Sigma Aldrich, potassium chloride (KCl, 99 %) from VWR and calcium chloride ($CaCl_2 \times 2H_2O$, a.r.), magnesium chloride ($MgCl_2 \times 6H_2O$, 99 %), D-glucose ($C_6H_{12}O_6 \times H_2O$, 99 %) from Molar Chemicals. *The composition of aCSF can be found in another article* [25]. Human serum (from human male AB plasma, USA origin, sterile-filtered) as a matrix material was from Sigma Aldrich. For the sensing measurements, kynurenine pathway molecules L-tryptophan (Trp, 1, 98 %) and nicotinamide adenine dinucleotide (NAD, 10, for biochemistry, 97 %) were provided by Merck GmbH, while kynurenic acid (Kyna, 2, 98 %), xanthurenic acid (XA, 3, 96 %), DL-kynurenine (Kyn, 4, 95 %), 3-hydroxy-DL-kynurenine (HKyn, 5, 98 %), 3-hydroxyanthranilic acid (3-HAA, 6, 97 %), anthranilic acid (AA, 7, 98 %), picolinic acid (PA, 8, 99 %) and quinolinic acid (QA, 9, 99 %) were from Sigma Aldrich. Serotonin pathway molecules 5-hydroxy-L-tryptophan (HTrp, 11), serotonin (HTA, 12, 98 %), N-acetyl-serotonin (ASer, 13, 99 %), melatonin (Mel, 14, 98 %) and L-tryptamine (TA, 15, 97 %) were supported by Sigma-Aldrich. *(Numbers after the names of the molecules correspond to the notations used in sensing studies, see Chapter 2.9.).* All solutions were prepared using Milli-Q ultrapure water (18.2 MΩ cm at 25 °C), and the reagents were used without further purification.

2.2. Preparation of transferrin-stabilized noble metal nanoclusters

2.2.1. Tf-AuAg NCs

The synthesis of the Tf-AuAg NCs was performed based on the method for Tf-Au NCs with some modifications [17]. In the finalized process, 5.4 mg Tf was dissolved in 960 μL water for 15 min, then 35.8 μL $HAuCl_4$ (10.0 mM) and 4.2 μL $AgNO_3$ (10.0 mM) stock solutions were added as metal precursors, obtaining a gold-to-silver ratio of 8.5:1. After 5 min of gentle stirring, the sample pH was raised over 12 by adding 100 μL of 1 M NaOH solution to initiate the reduction of metal ions by promoting the reducing effect of the Tf. The sample was left in the dark at room temperature for 24 h without stirring, finally obtaining the orange-red-emitting NCs. For larger volumes, the quantities were simply multiplied.

2.2.2. Tf-Au NCs

To compare the optical properties, the protein structural changes and the results of the sensor studies of the newly synthesized Tf-AuAg NCs, Tf-Au NCs were also fabricated by our protocol. The preparation was started by dissolving 1.5 mg of Tf in 920 μL of water for 15 min, then 80 μL of 10.0 mM $HAuCl_4$ solution was added and left stirring for 5 min. Subsequently, the sample pH was increased by the addition of 100 μL of 1 M NaOH solution over 12. The final nominal concentrations were Tf at 1.36 mg/mL and Au at 0.73 mM. After 5 min of mixing, the sample was put on a hot plate providing 40 °C during the subsequent 24 h. The sample was left still during this step and was protected from ambient light. The resulting Au NCs showed intense red emission at 628 nm and were used in the abovementioned experiments.

2.2.3. Purification of the cluster's dispersion

The subsequent cleaning of the NCs was performed using dialysis. One sample was first diluted with water to 4.6 mL, then inserted into a 14 kDa molecular weight cut-off cellulose membrane and dialyzed against 1 L Milli-Q water for 1.5 h, which proved sufficient for the elimination of contaminants and residual salts. The complete

purification was achieved by a second dialysis step, changing the spent matrix for a fresh batch of water and continuing the process for another hour. The purified samples were then stored in the fridge, protected from light, until further use.

2.2.4. Preparation of solid samples from dispersions

For characterization, solid samples were prepared by freeze-drying the purified aqueous dispersions of bimetallic NCs. First, the nanocluster dispersions were frozen using liquid nitrogen, and then they were transferred to a Flexi-Dry™ (FTS Systems®, Inc.) lyophilization instrument for 24 h to evaporate all the solvent.

2.3. Fluorescence measurements

Fluorescence of the samples was investigated using a Jasco FP-8500 fluorimeter. The samples were transferred into a 10 mm quartz cuvette and were measured applying 2.5 nm slit values for both excitation and emission monochromators with a 200 nm/min scan speed. 3D spectra of optimized Tf-AuAg NCs were recorded ranging $\lambda_{ex} = 200-500$ nm and $\lambda_{em} = 210-800$ nm using the same device applying a 500 nm/min scan speed. Quenching studies and fluorescence sensing measurements were performed on a Horiba Jobin Yvon FluoroMax-4 spectrofluorometer. On this device the applied slit values were 3 nm for nanocluster samples and 2 nm for pure protein. Fluorescence quantum yield measurements were performed using an integrating sphere (Jasco ILF-835 with 100 mm diameter). Quantum yield calculation was performed using the built-in software of the Jasco FP-8500 spectrofluorometer based on three recorded spectra: direct excitation, where the exciting beam hits the sample directly; indirect excitation, where the beam hits the wall of the integrating sphere and only diffused light excites the sample; and a spectrum recorded without a sample for the measurement of scattered light. The measured spectra were corrected using a Jasco Calibrated Light Source-WI (ESC-842) without using other references. Calculations were made by the ABL&E JASCO SpectraManager 2.0 software provided with the fluorimeter. Fluorescence lifetime measurements were executed using a Horiba DeltaFlex time-correlated single photon counting (TCSPC) device. Multiple samples were analyzed in a 10 mm quartz cuvette using a DeltaDiode pulsed laser as a light source ($\lambda = 371$ nm), and a 400 nm longpass filter was employed. All measurement data were registered using a 50 kHz repetition rate in the range of 0–13 μs, with a wide slit value of 12 nm due to the long lifetime components and relatively low quantum yields. The instrument response function (IRF) was measured with multiple settings for the correction of very short lifetimes using a standard silica dispersion provided by Horiba. The decay curves were evaluated using the EZTime program included with the device. The measurement data were fitted using exponential functions and the lifetime components were determined, while the fitting was characterized by the obtained χ^2 values.

2.4. Ionic strength and pH dependence studies

The optical and colloidal stability of NCs were tested against different NaCl concentrations and in the range of pH = 1−13. To obtain a sample, 1.8 mL of sodium chloride solutions with different concentrations were prepared from a stock solution (1 M) and 200 μL of NCs were added while stirring, reaching ionic strengths ranging 0−0.5 M. For pH experiments, the solution pH was adjusted using hydrochloric acid and sodium hydroxide solutions, applying 0.1 M NaCl for constant ionic strength during the measurements. The hydrodynamic diameter of the protein-stabilized NCs was measured using a Malvern ZetaSizer NanoZS ZEN 4003 instrument equipped with a 633 nm He–Ne laser, applying a 173° scattering angle for detection. Five parallel measurements were made using 2-min temperature regulation at 25 °C.

2.5. Fourier-transformed infrared spectroscopy (FT-IR)

FT-IR spectra of Tf and Tf-AuAg NCs were registered using a Jasco FT/IR-4700 device with an ATR PRO ONE Single-reflection accessory. IR data were measured in the range of 500–4000 cm^{-1} with 1 cm^{-1} resolution, and 16 interferograms were cumulated for one spectrum. Measurements were made on the powder obtained from the successive dialysis and lyophilization of pristine Tf and Tf-AuAg NCs samples.

2.6. Circular dichroism (CD)

Circular dichroism spectra of Tf, Tf-Au NCs and Tf-AuAg NCs were measured using a JASCO J-1100 spectrometer. Individual samples were diluted to 6.5×10^{-2} mg/mL (Tf1 and Tf-Au NCs) and 5.9×10^{-2} mg/mL (Tf2 and Tf-AuAg NCs). The ΔAbs of the samples were registered in the 200−300 nm range using 1 cm optical length at ambient temperature. The sample compartment was constantly purged with N_2 applying 3 L/min speed. The ratio of secondary structure elements was calculated by fitting the measured data (in molar ellipticity units) using the Reed model in the Jasco SpectraManager 2.0 Secondary Structure Estimation software.

2.7. Transmission electron microscopy (TEM)

TEM images were recorded using a FEI-Tecnai G2 20 X-Twin High-Resolution Transmission Electron Microscope applying 220 kV voltage. The electron source of the device was a heated W filament. The samples were diluted and dropped on a carbon mesh grid, followed by a gentle drying using an infrared lamp. Bright-field images were recorded at 255 kX magnification and size distribution was calculated with ImageJ software.

2.8. Quenching studies

The fluorescence quenching on Tf and Tf-AuAg NCs was tested using iodide ions, which are known to efficiently quench the emission of Trp. In a series of experiments, 0.1 M KI solution was added in different volumes (0−125 μL) to a mixture of PBS and protein or Tf-AuAg NCs dispersion (250 μL) reaching a total volume of 2.5 mL. The quenching effect was simply evaluated based on the excitation and emission spectra of the samples.

2.9. Sensing of tryptophan metabolites

The effect of the kynurenine and serotonin pathway molecules on Tf-AuAg NCs' fluorescence was checked in three different media. In a typical measurement, 250 μL of NCs' dispersion was diluted with the medium (PBS, aCSF or diluted human serum, where the stock was diluted five times with PBS), then 86 μL of neuroactive molecule solution was added to reach 34.4 μM concentration in a total volume of 2.5 mL per sample (the molar ratio of metal content to neuroactive molecule was 1:3.96, for protein it was 1:23.3). The stock solutions of the tryptophan metabolites (molecules 1−15) were freshly made by dissolving the dry powder in the appropriate medium (PBS for the human serum samples) to reach 1 mM final concentration. In the case of 3-hydroxyanthranilic acid (3-HAA, molecule 6) further samples were prepared by varying the added volume (10−200 μL) and the concentration of the stock solution (0.1 or 0.01 mM), in the range of 0–34.4 μM in PBS and aCSF only.

2.10. Isothermal Titration Calorimetry (ITC) studies

The interaction between 3-HAA and Tf was checked with Isothermal Titration Calorimetry (ITC) measurements using a VP-ITC microcalorimeter from MicroCal Inc. (Northampton, MA, USA). During the calorimetric experiments, 10 μL of the 3-HAA solution was injected in 25

increments into 1.4 mL of the Tf solution with constant stirring. Each injection of the 3-HAA solution was administered for over 20 s, followed by a 200-s interval before the next injection. To account for the dilution effect in the recorded enthalpograms, corresponding reference blank trials were performed under identical conditions. Specifically, the titration of the 3-HAA solution in PBS was carried out with 10 μL of the ligand solution in 25 steps into 1.4 mL PBS. To prevent bubble formation, all samples were degassed for 10 min shortly before the measurements began. The sample cell was continuously stirred at a rate of 240 rpm, and the experiments were conducted at 25 °C. The thermal information (dQ/dt) collected during the calorimetry was displayed on differential calorimetric curves registered as a function of time. The acquired enthalpograms showed enthalpy change values related to the amount of 3-HAA added to Tf as a function of the molar ratio (ligand/protein) attributable to each dosing step. The heat effect resulting from the dilution of the ligand was corrected with the results of reference blank tests. In similar tests, Tf-AuAg NCs with identical protein concentrations were also used to check the effect of nanocluster formation on the binding interaction.

3. Results and discussion

3.1. Optimization of the synthesis protocol of the bimetallic nanoclusters

The Tf-AuAg NCs possessing the highest fluorescence were chosen based on a protocol similar to our previous works [25,26]. In short, parameters such as the gold-to-silver ratio, Tf and metal concentration, temperature as well as synthesis time were varied to reach optimal fluorescence. The results of optimization are summarized in Fig. 1. In the first step, some of the gold solution was changed to 10.0 mM $AgNO_3$ ranging from 4:1 to 15:1 gold-to-silver molar ratio. The NCs prepared this way showed lower fluorescence compared to Au NCs, about halving the intensity (from 4000 to ~2200), but a clear maximum could be detected in this region at 8.5:1 ratio (Fig. 1 A). The next step was changing the Tf quantity (thus concentration) of the samples in the range of 1.2–6.6 mg per sample (1.09−6.00 mg/mL, see Fig. 1 B). The addition of extra protein as reducing agent doubled the fluorescence of the NCs when the Tf content was at 5.4 mg (4.91 mg/mL). Further increase did not cause any significant improvement. The effect of temperature was checked at multiple points in the range of 10–60 °C. Based on the results, the ambient temperature was ideal for synthesis providing a remarkable increase in fluorescence and a blue shift in emission (Fig. 1C). Near room temperature syntheses (17–32 °C) provided similar intensities with low variation in emission maxima (±1–2 nm), thus any heating or cooling results in similar or lower emission, therefore should be avoided. Higher temperature induces slight denaturation of the protein, which results in lower reducing capacity and an emission profile closer to the original Au NCs. The metal concentration was altered from 0.22 to 2.22 mM. Comparing sample emission intensities (not shown) there is no improvement for any sample, only the sample with 1.09 mM metal concentration (1.5 times) shows a similar (slightly lower) value. However, checking the normalized emission (intensity per mM of metal) showed a significant escalation peaking at 0.36 mM with a ~60 % rise accompanied by a red shift from 599 to 606 nm (Fig. 1 D). Synthesis time had a large effect on sample fluorescence, as shown in Fig. S1. After increasing the pH to 12, the NC formation slowly started with a maximum at 580 nm in the first 60 min, then the fluorescence rapidly escalated followed by a red shift to 613 nm after 2−2.5 h. The peak assigned to protein emission rapidly decreased during the first hour, supposedly due to the disappearance of a blue-emitting intermediate or the effect of quenching caused by the presence of the forming NCs. The peak position of the NCs remained almost intact with the passing time, while emission amplification lessened after 4 h, and after 12 h reached a steady value. The highest fluorescence was obtained at 18 h, but for subsequent work 24 h was considered optimal as it provided adequate emission and flexibility with performing the synthesis. The final bimetallic NCs were compared to the original monometallic NCs plus another sample prepared using the optimized conditions (with 40 μL of $HAuCl_4$ stock solution instead of a mixture with $AgNO_3$). As displayed in Fig. S2, optimization shifted the emission

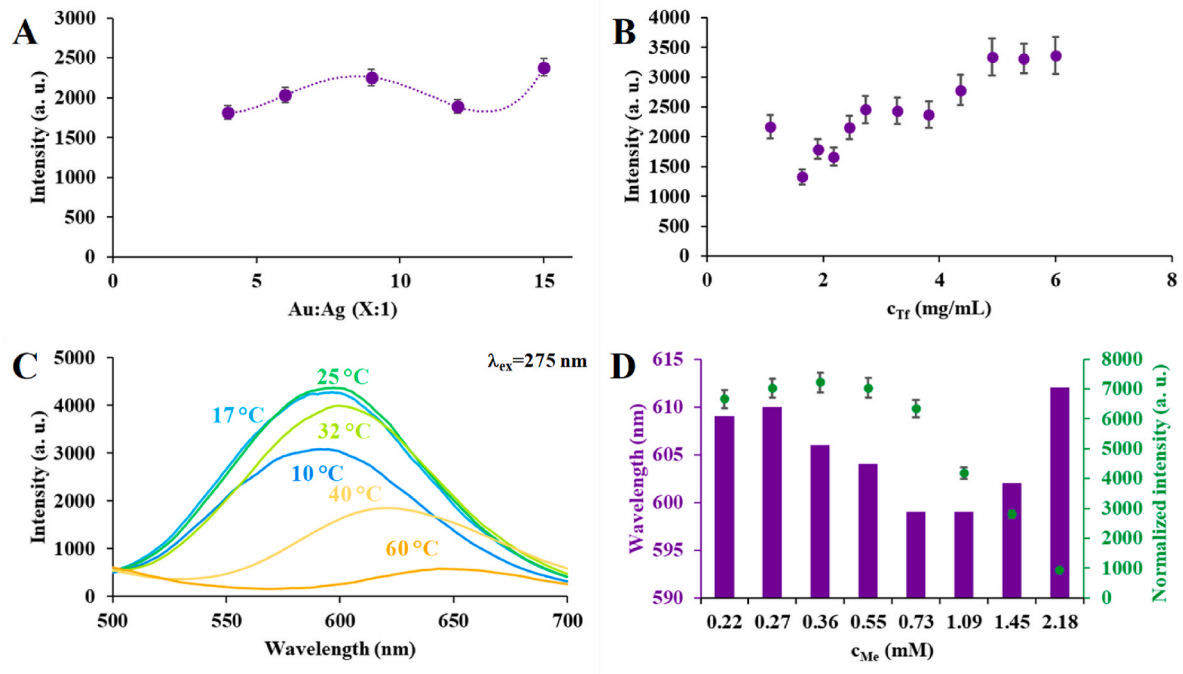

Fig. 1. Optimization of the experimental parameters for the preparation of bimetallic NCs: The effect of gold:silver molar ratio at 0.73 mM metal concentration **(A)** (c_{Tf} = 1.36 mg/mL, T = 40 °C), the Tf concentration **(B)** ($c_{metal\ ion}$ = 0.73 mM, c_{Au} = 0.65 mM, c_{Ag} = 7.7 × 10^{-2} mM, T = 40 °C), the synthesis temperature **(C)** (c_{Tf} = 4.90 mg/mL, c_{Au} = 0.128 mg/mL, c_{Ag} = 8.3 × 10^{-3} mg/mL) and the total metal concentration **(D)** (c_{Tf} = 4.90 mg/mL, T = 25 °C) on the fluorescent emission intensity. λ_{ex} = 275 nm.

from 626 nm to 595 nm and amplified the intrinsic emission by more than 4-fold. Monometallic NCs prepared with the optimized parameters showed worse emission values compared to both the original NCs and the optimized ones (58 % emission compared to original Au NCs at 652 nm), clearly showing the importance of the introduced silver atoms on fluorescence.

3.2. Characterization of NCs

3.2.1. Optical properties

3.2.1.1. Evaluation of 3D spectra. Characterization of the bimetallic NCs was performed after purification according to the protocol presented in Chapter 2.2. The registration of a 3D spectrum could help in the identification of fluorescent processes composing the final emission spectra obtained at different excitation wavelengths. Based on the excitation and emission values presented in Figure S3 A, we could separate individual peaks that are present in the spectra. First, peaks related to the Tf and the NCs are obviously separated in the emission spectra with different excitation values assigned to each peak. Emission peaks of Tf appear below 500 nm and mainly come from Trp present in the protein. The peaks are at higher values compared to the pure Tf emissions (see Figure S3 B). This is apparently the result of the cluster formation which makes the protein emission peaks much weaker (34 % loss) with a significant red shift from 330 to 350 nm. For the NCs this means that the presence of the metal atoms or a change in secondary protein structure alters the emission of Trp residues, which become more susceptible for quenching caused by solvent molecules, causing the abovementioned red shift [27]. This region consists of at least two different peaks centered around $\lambda_{em} = 360$ nm ($\lambda_{ex} = 280$ nm) and $\lambda_{em} = 405$ nm ($\lambda_{ex} = 325$ nm). The second peak is much weaker compared to the first one and is only present as a weak shoulder on the excitation spectra, but it is much more accentuated on emission spectra (hidden by the NC peaks in Figure S3 A). If we compare the spectra of Tf and NCs focusing on the protein-related or the NC peak (as presented in Fig. S4) we can see that the shape and positions of excitation change. The peak of NCs does not change its shape significantly, but the peak maximum shifts from 600 to 590 nm with higher excitation wavelengths. Combined with the time dependence studies (Fig. S1) we can surmise that the NC emission is the sum of multiple smaller peaks with different emission maxima.

3.2.1.2. Quantum yield measurements. Measurements performed on gold and bimetallic NCs revealed acceptable quantum yield values of 4.21 (±0.15) % for gold and 3.46 (±0.30) % for bimetallic NCs, respectively. X. L. Guével et al. also reached 4.3 % for Tf-Au NCs, but during synthesis ascorbic acid was also applied to help reduction [24]. Compared to other protein-stabilized NCs in the literature [25,28] the resulting material performs relatively well (2.31 % for γ-globulin-, 2.5 % for bovine serum albumin- and 4.8 % for lysozyme-stabilized AuAg NCs), yet they have much lower quantum yield when compared to NCs made with the microwave method or by using an additional reducing agent (10.44 % and 9.16 %, respectively [17,18]). Nevertheless, this value was sufficient to perform all the experiments of this work, even after tenfold dilution.

3.2.1.3. Fluorescence lifetime. Measuring the lifetime of the fluorescence processes is a good method to find out the source of the individual emission peaks. We successfully recorded the emission decays of gold and bimetallic AuAg NCs and fitted the data assuming 3 lifetime components (τ_1–τ_3, see Fig. 2). Most of the emission (~75–80 %) comes from the largest component, which is 2.20 μs for gold and 1.56 μs for AuAg NCs at their apparent emission maxima (640 and 580 nm, respectively; the wavelengths are different from the earlier presented values due to the change of the measurement device). Based on the value itself, this process should be phosphorescence rather than fluorescence as indicated in many publications [29,30]. Other components have less contribution, which is 17–20 % for τ_2 (410 and 250 ns) and a very small value for τ_3 (11.8 and 8.2 ns with contributions of 2.4 and 4.9 %). If we check the lifetime values and contributions at different wavelengths (610, 660 and 710 nm), we can see that they change in accordance with the emission wavelength. Lifetimes become longer at higher wavelengths, which is expected due to the longer time needed for these processes to conclude. The contributions are connected to the individual processes, which possess their own emission maxima as discussed previously. The first component has a much higher contribution (82.6–95.3 %), while the others decrease (τ_2: 11.1 %–4.1 %; τ_3: 6.3 %–0.6 %). Due to the shortage of data, we can only know that the first two components are assigned to the cluster emission peak while the third one

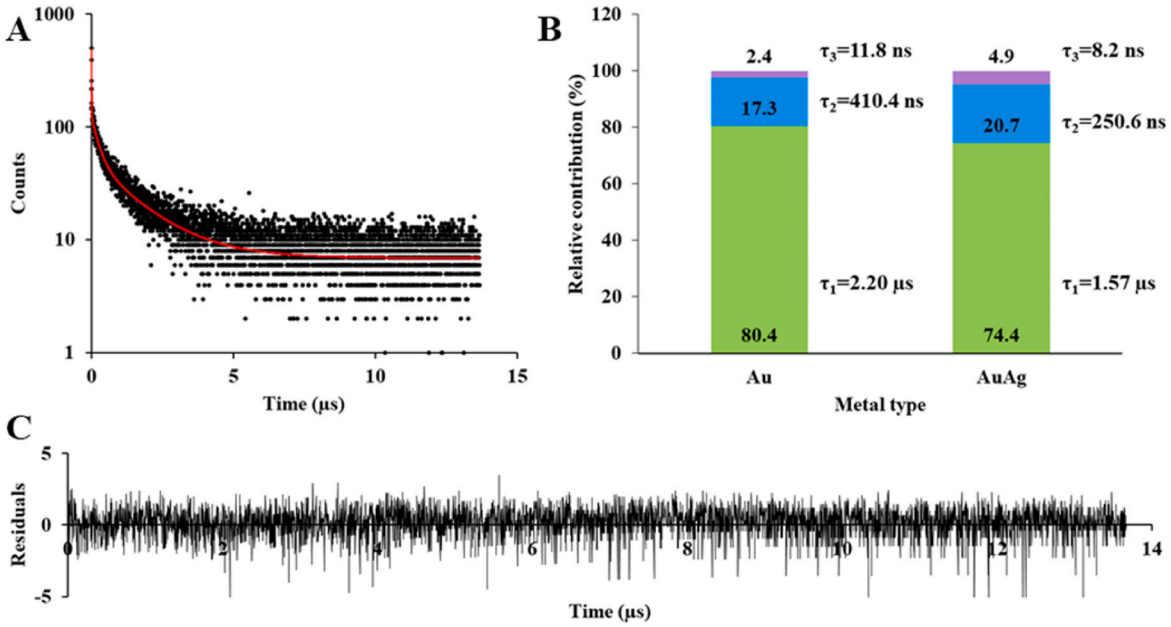

Fig. 2. Fluorescence lifetime decay and fitted curve of Tf-AuAg NCs **(A)** The contribution of the lifetime components in gold and bimetallic NCs (**B**). Residual of the presented multiexponential fitting method (**C**) $\lambda_{ex} = 365$ nm.

belongs to ligand-related processes. Furthermore, we can assume that τ_2 and τ_3 have their emission maxima below 660 nm based on the changing contribution values. If we deconvolute the emission spectrum recorded with this measurement, we can divide it into 3 peaks. The first one is only the high wavelength end of the protein peak with a maximum of ~444 nm (the fitting of this peak is largely based on extrapolation so the value can be very different). This peak can be coupled with the fluorescence of Trp, with the ns lifetime of τ_3 which causes much of the Tf emission [27]. The next peak is centered at 583 nm with a decline in the measured region (610−710 nm), which means that this is paired with τ_2. Based on the value itself, this can be the metal-to-metal charge transfer happening in the NC cores [26,31]. The last peak with a maximum of 669 nm is assigned to τ_1, which is the ligand-to-metal or ligand-to-metal-metal type charge transfer characteristic of protein-stabilized metal NCs [32,33]. The highest occupied molecular orbital (HOMO) should consist of the p orbitals of the ligands (e.g. through the Au–S bond). The lowest unoccupied molecular orbital (LUMO) should be from the d orbitals of the core metals (Au and Ag). The change of the NC cores can influence the charge transition, as there is less sd hybridization in Ag (5s) compared to Au (6s) due to relativistic effects, which means higher energy levels for the LUMO, therefore the energy gap widens, resulting in the blue shift of the λ_{em}. As a matter of fact, these are only the minimally separated emissions; multiple core structures can be imagined based on different Au:Ag atomic ratios which must have different emission peaks and lifetimes, however due to the insufficient resolution of the technique and the lack of measurement data, no more information could be extracted. If we consider the process of the suspected phosphorescence, higher quantum yield can be explained by a faster transition between the singlet (S_1) and triplet (T_n, usually T_1 or T_2) states [34]. If we assume that the incorporation of Ag lowers the energy gap (ΔE of the $S_1 \rightarrow T_n$ process) between the appropriate states, the efficiency of phosphorescence becomes higher compared to internal conversion channels, thus the measurable QY% increased.

3.2.2. ICP-MS

The applied purification process following the synthesis can change the actual metal content of the NCs. In most publications, no data can be found for the exact metal concentration of the prepared nanostructured materials. To determine the metal content, ICP-MS measurements were performed on gold and bimetallic NCs. The results are summarized in Table 1. Comparing the nominal (total) and measured (actual) data for both Au and Ag, we can see that gold content decreased by 25.2 % for monometallic NCs and by 22.1 % for bimetallic NCs. Presumably, not all the gold ions were reduced, and during the purification process, the excess ions were removed by dialysis. Silver content showed an increased value, most probably the volume of the sample decreased during the synthesis (24 h) due to the slight evaporation of the solvent or the nominal content was more. We can suppose that the silver content does not change significantly, which would be in accordance with our previous work [26]. The actual gold-to-silver molar ratio therefore changed from the original 8.51:1 to 5.65:1. This corresponds to $Au_{85\ \%}$ – $Ag_{15\ \%}$ percentage element ratio.

3.2.3. TEM studies

While X-ray photoelectron spectroscopy investigations were not carried out to confirm the zero-oxidation state of the elements in the final products, the registered transmission electron microscopy images strongly support the formation of NCs. The captured images (Fig. 3) revealed that the diameter of NCs is around 2.0 (±0.3) nm with a very narrow distribution, as the majority (~75 %) is in the range of 1.67–2.33 nm. The NCs usually take a spherical shape and are quick to melt due to the energy of the applied electron beam; therefore, the actual size can be somewhat underestimated. Compared with the results from dynamic light scattering ($d_H = 7.2 \pm 0.6$ nm), we clearly observed a smaller average size, as DLS is sensitive to the hydrodynamic diameter of the particles while TEM measures the NC cores in their dry state, as published previously for other metallic NCs [24,26].

Table 1
Calculated and measured concentration of metals in pure gold and bimetallic NCs.

	Nominal concentration (μg/mL)		Measured concentration (μg/mL)	
NCs type	Au	Ag	Au	Ag
Au	68.50	–	51.20	–
AuAg	15.30	0.985	11.92	1.156

3.2.4. FT-IR

Fourier-transformed infrared spectra of Tf and Tf-AuAg NCs were registered to check the effect of NC formation on the protein structure. The FT-IR spectrum for Tf-Au NCs is already available in the literature [24]. Based on our results (Fig. 4 and Table 2), the NCs show similar peaks as the initial protein, with very few changes in peak positions and area ratios. The most noticeable change is the rise of the amide I peak at ~1640 cm^{-1} compared to the amide II peak at 1570 cm^{-1}. Some peaks at lower wavenumbers also show higher absorbance (e.g. 1395, 835 cm^{-1}) but these could not be assigned to exact bonds as they appear in the fingerprint region of the spectra. Checking the amide I peak, we can resolve the peaks based on previous publications [26,35], where the different secondary structure elements present in Tf belong to different energy (wavenumber) absorptions. Comparing the peak areas belonging to each structural element, we can see that the formation of NCs mainly reduces the ratios of α-helices and β-sheets while the β-coils and random structures are enhanced, as shown in Table 2. This change is explained by the structure deformation caused by the interaction between the metal atoms and Tf, which is further complicated by the reduction and self-assembly of Au and Ag atoms and the formed NCs taking up larger space in the Tf structure. Additionally, the stabilizing Au–S bonds and the oxidized Tyr ligands also distort the structure. A similar conclusion was obtained in the case of Tf-Au NCs [24], so varying the composition of the metallic core does not significantly change the cluster formation mechanism and thus the protein matrix structure.

3.2.5. CD

Circular dichroism measurements of the free protein and mono- and bimetallic NCs reveal the disrupting effect of nanocluster formation on protein secondary structure, as shown in Fig. 5 and Table 2 for the Reed model. CD data for the formation of Tf-Au NCs was not available in the literature; thus, all derivatives were analyzed and compared at similar concentrations (0.059 and 0.065 mg/mL). Raw data was evaluated using both the Yang and Reed models, where the former showed better fitting for the Tf, but completely failed in determining the structure for NCs, so the Reed model was used for this article. Transferrin has a sizable amount of ordered structural elements, such as α-helices and β-sheets (~12 and 45 %) which show smaller contributions in the NCs (~0 % of α-helices and 38−41 % of β-sheets for both NCs). The calculations showed similar trends as FT-IR measurements, except β-coils and random structure ratios were mixed, which is due to the differences in these methods and the evaluation of the data.

3.2.6. Stability studies

The optical and colloidal stability of the NCs were checked in different ionic strength and pH conditions. As displayed in Fig. 6, samples reacted with a slight increase in fluorescence when the ionic strength was raised from 0 to 0.05 M, then showed a slow decline onwards to 0.5 M. This effect was possibly related to minor aggregation between the NCs, but DLS measurements did not reveal significant size change due to ionic strength (7.9 ± 0.4 nm measured in PBS compared to the original 7.2 ± 0.6 nm in water). In the case of pH, sample fluorescence remained relatively stable in a broad range, the only exceptions being pH = 1−2 and around the protein isoelectric point (IEP). Very

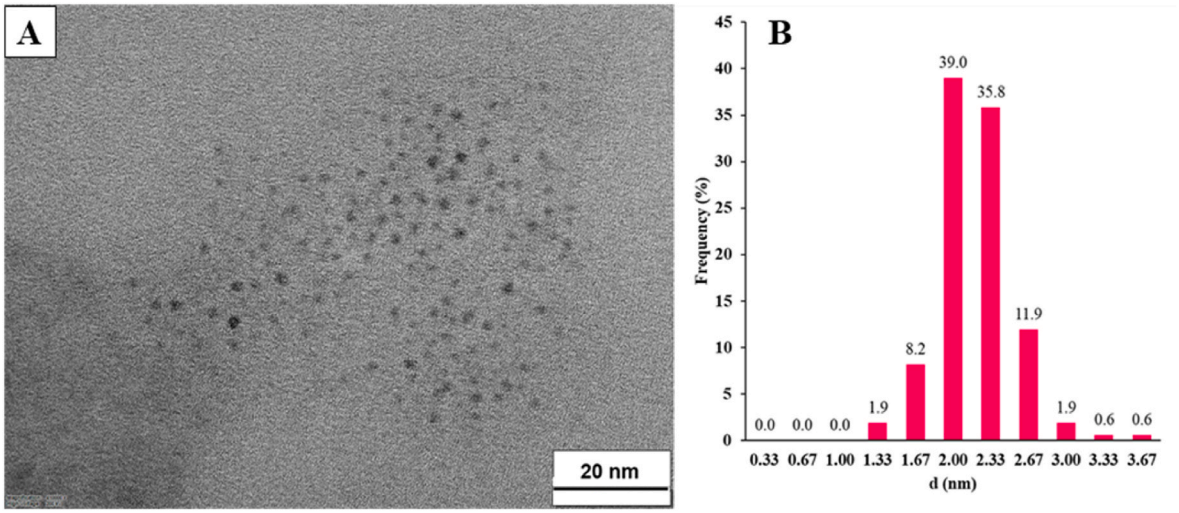

Fig. 3. Transmission electron microscope image of Tf-AuAg NCs **(A)** and the size distribution of the NCs based on the captured image **(B)**.

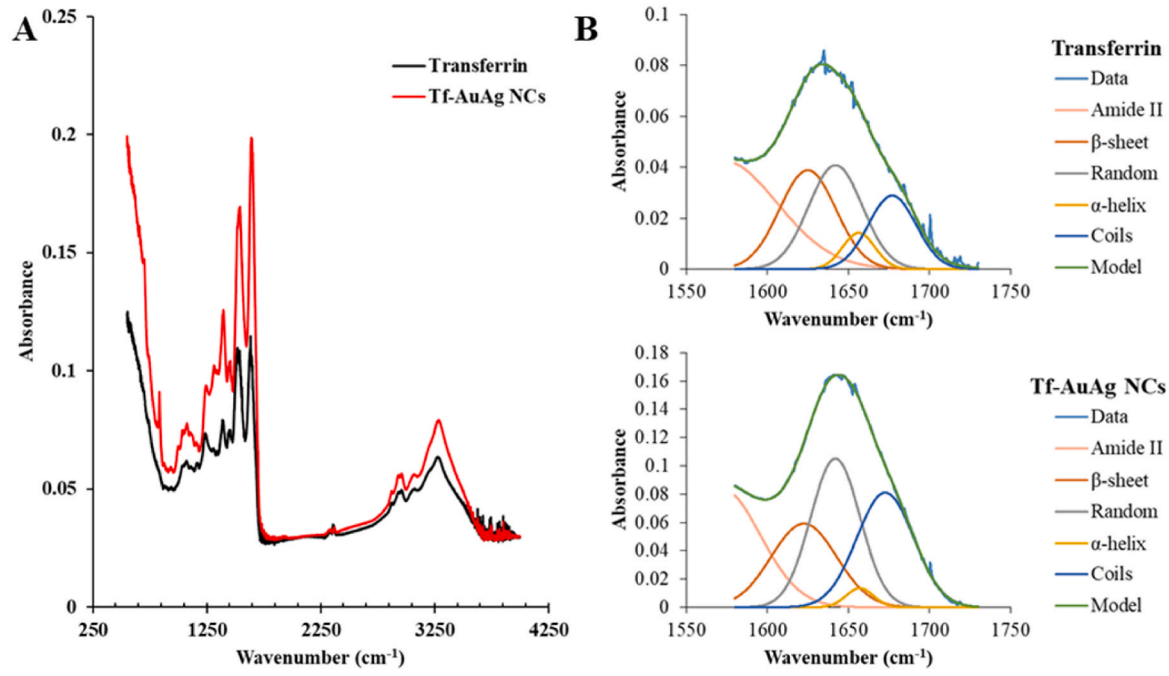

Fig. 4. FT-IR spectra of pure protein and Tf-AuAg NCs under same pH conditions **(A)** and the deconvolution of the amide I peak for Tf **(B)** and Tf-AuAg NCs **(C)** based on literature [35].

Table 2
Evaluation of Tf secondary structure based on FT-IR (top) and CD data (bottom, calculated using the Reed model).

FT-IR	α-helix	β-sheet	Coils	Random	
Tf	7.4	34.4	22.2	35.9	
Tf-AuAg NCs	2.7	27.5	32.8	37.0	
CD	**α-helix**	**β-sheet**	**Coils**	**Random**	**RMS**
Tf	12.3	44.8	6.7	36.2	10.063
Tf-AuAg NCs	0.4	41.3	5.1	53.2	5.385

acidic conditions disrupt the protein secondary structure as well as provide the chance for silver atoms to be dissolved, therefore decreasing the emission and shifting it towards the red region. In contrast, the NCs aggregate near the IEP of Tf due to their low stability in these conditions; thus, their fluorescence is amplified due to the aggregation-induced enhancement phenomenon (AIE) [29,30]. While it is evident from the image of the samples that there is a significant aggregation at pH = 4 and 5, subsequent light scattering measurements performed on a new set of samples could not reveal any relevant changes in size, which means that noticeable aggregation is restricted to a small pH range. To summarize, pH over 6 should be appropriate for working with NCs even at relatively higher ionic strengths (0.1 M), which is also in accordance with the literature [24], where neutral and basic conditions are suggested.

3.2.7. *Quenching studies*

The quenching of the fluorescence of NCs usually involves electron transfer, formation of a complex between the NC and the quencher or simply oxidation of the metals [26,36]. The fluorescence quenching of pure Tf and Tf-stabilized bimetallic NCs was performed using potassium

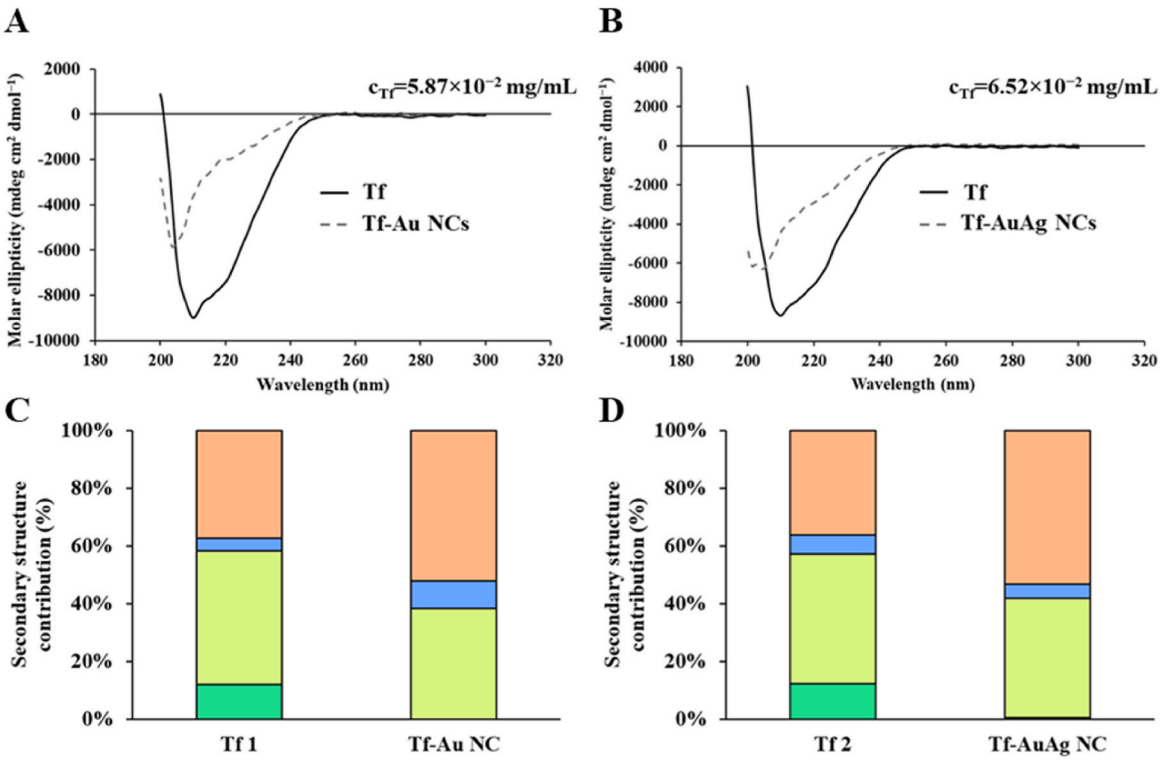

Fig. 5. Circular dichroism spectra of Tf-Au NCs (grey, dashed) **(A)** and bimetallic NCs (grey, dashed) at 25 °C **(B)**. Both spectra contain the spectrum of pure Tf protein (black, straight) for comparison. Assessment of secondary structure elements based on the Reed model [26] for Tf-Au NCs **(C)** and for Tf-AuAg NCs **(D)**.

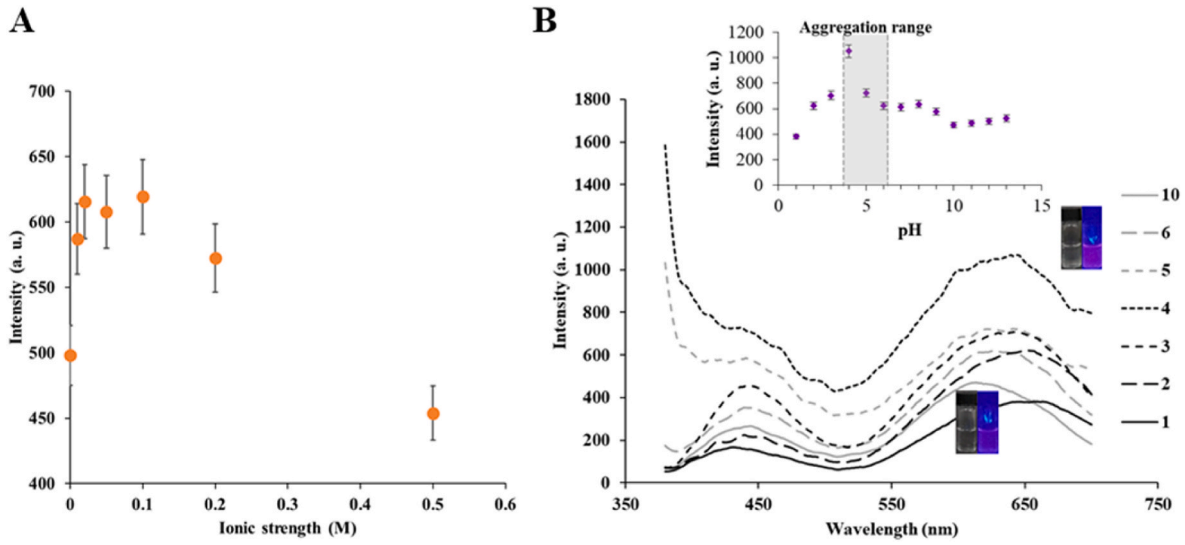

Fig. 6. Effect of ionic strength **(A)** and pH **(B)** on the emission intensities of the NCs. Representative photos of the aqueous samples at pH = 4 (bottom) and at pH = 10 (top).

iodide (KI) solutions. I^- is a well-known quencher of Trp which provides the majority of Tf emission around 330 nm [27]. Different concentrations of KI ranging 1−5 mM were added to Tf and Tf-AuAg NC samples in PBS buffer. Based on the measurements displayed in Fig. S5, the presence of I^- slightly decreased the overall Tf emission. Comparing the excitation spectra reveals minor changes mainly in the region of 240–260 nm. In the case of bimetallic NCs, the presence of I^- decreases the emission in the blue region and there is a significant blue shift taking place here. The fluorescence of NCs in the red region is somewhat enhanced, with a larger effect on the peak around 670 nm. Examining the corresponding excitation curves we can observe that the I^- ions decrease excitation at lower wavelengths (similar for Tf, between 240 and 260 nm). In turn, excitations over 300 nm (belonging to NCs emission) are stronger. Based on these results, we can assign excitation-fluorescence peaks independently from 3D fluorescence measurements. The fact that quenching was induced by I^- means that the fluorophores responsible for the emission at 450 nm are accessible for these ions, therefore they are closer to the surface of the NCs. These species encounter the solvent molecules, which reduce their emission compared to species embedded in the protein and cause a red shift due to the energy loss coming from fluorophore-solvent interactions. Additionally, selective enhancement at the NC peak means that the

ligand-related peak around 670 nm (with τ_1 lifetime) is more sensitive to the presence of I^-, which is not surprising, considering that the metal cores are embedded deeper in the protein structure.

3.3. Sensing of kynurenine pathway molecules

In the sensing measurements, 10 different molecules from the kynurenine pathway were tested first (Fig. S6 and S7). Based on the results presented in Fig. 7A, we found that only 3-hydroxyanthranilic acid (3-HAA, marked as 6) caused a significant change in fluorescence compared to the pure Tf-AuAg NCs (marked as 0) in PBS medium ($I/I_0 \sim$ 1.6–1.7). Other molecules only had a minuscule effect, usually shifting the maximum of fluorescence due to their own blue emission. The only exception was 3-hydroxy-DL-kynurenine, where the shape of the emission curve changed, mainly because of an increase for the lower energy part of the NC emission (belonging to the τ_1 lifetime emission at ~670 nm). In the case of 3-HAA, the signal was checked in the range of 0–34.4 μM and we could determine its limit of detection (LOD) value at 0.55 μM (Fig. 8A and Fig. S8A). At higher concentrations the self-fluorescence of 3-HAA can overlap with the emission of the NCs, but this effect is negligible in the region of detection. The growth of emission can be generally explained by aggregation-induced enhancement (AIE). In opposition to the sensing mechanism presented for serotonin in the literature [17], only a minor aggregation might occur between the NCs in our case, as we could observe neither large-scale aggregation nor the formation of stable light-scattering particles due to the presence of 3-HAA with DLS (size with 34.4 μM of 3-HAA was 7.0 ± 0.7 nm compared to the original diameter of 7.2 ± 0.6 nm). The presence of 3-HAA can make the protein structure more rigid, resulting in the partial inhibition of non-radiative decay processes, therefore amplifying the emission of fluorescent photons. The effect of 3-HAA was also checked for fluorescence lifetime-related changes. Due to the overlapping of fluorescence signals, τ_3 became the mixture of the protein and 3-HAA fluorescence, and the larger contribution based on concentration was also evident. The NC-related lifetimes showed a declining contribution, and their values were also smaller. This could be a result of different measurement parameters, which affected the larger lifetime components more, or it could be due to the presence of the 3-HAA.

Similar experiments were also conducted in an aCSF medium with different results. The medium itself had an enhancement effect on the fluorescence of NCs (around 10−15 % increase compared to water), which did not disturb the sensing reaction. This change might be caused by the Ca^{2+} and Mg^{2+} ions present, which might bind to the stabilizing protein of the NCs, thereby restricting non-radiative decay [37]. The investigated kynurenine pathway molecules further raised the emission regardless of their structure, and selective enhancement appeared only for some molecules, namely xanthurenic acid (XA), DL-kynurenine (Kyn), HKyn, and 3-HAA. Kyn does not show much any effect in PBS, it only has an emission peak overlapped with the Tf emission (around 470 nm), but in aCSF greater enhancement can be detected, especially at lower wavelength NC-emissions (λ_{em} = 525–625 nm, see Fig. S7). This part of the peak might increase due to some kind of complex formation with one of the constituents of aCSF, and overlaps much more with the NC peak, shifting and increasing the fluorescence below 630 nm. The spectrum over this wavelength is the same as for molecules with no effect on emission, thus selective emission strengthening can be excluded. For 3-HAA, the sensing reactions showed a similar curve as in PBS, but the calculated LOD value was even lower (0.32 μM, see Fig. 8B and Fig. S8B). The linear region is very short, followed by a saturation-like curve showing maximization of fluorescence below 5 μM. As 3-HAA has its own fluorescence based around 420−430 nm, its concentration could be determined without the application of NCs. However, there are many interfering agents showing fluorescence in the blue region disrupting the determination of 3-HAA (such as AA), but in the emission region of the NCs (~610 nm) there are very few substances emitting, so this is ideal for experiments. The sensing studies were carried out with the pure Tf-Au NCs as well, and only slight enhancement ($I/I_0 \sim$ 1.1–1.2) could be observed, which means that our developed bimetallic NCs show higher sensitivity only for 3-HAA as a result of possibly better interaction.

In the final series of experiments, response of the NCs was also tested in diluted human serum (see Fig. 7A and S7). Our results showed that the biological matrix had negative effects on sensing, as the large protein content, scattering particles and aggregates hindered precise fluorescence measurements. Using a blank matrix without NCs as background, we could visualize the effects of the tested molecules on the NCs, which is shown in Fig. S7. In the presence of the serum, the NCs' emission profile changed drastically, with a large red shift ($\Delta\lambda$ = +38 nm) and increase in fluorescence (~21 %). However, when we added the tested molecules to the sample, the fluorescence shifted back near the NC-emission in water ($\Delta\lambda$ = − 30−35 nm), and the emission intensity was also lowered (−12−16 % compared to the signal in serum) regardless of the molecule. The results were similar to the data in aCSF, as remarkable difference was only detected in the case of XA and 3-HAA, where the intensity was higher compared to the other molecules; in the case of 3-HAA, the signal was also as large as the intensity measured for the NCs. Surprisingly, we detected the decrease of the emission in the case of Kyn, which did not happen in the other media. On another note, XA and HKyn decreased the emission of the proteins present in the samples (Tf and serum constituents), therefore the corrected spectra show negative values in the λ_{em} = 380−500 or 380−555 nm regions). As the presence of the serum greatly increased the detected intensity, the noise was also greatly enhanced (around 3-5 × in individual samples compared to the NCs in water), therefore the LOD value in serum ought to be much higher compared to the ones determined in PBS and aCSF.

The bimetallic NCs were also employed in sensing reactions with dopamine pathway molecules (5 molecules and Trp from the kynurenine pathway, Fig. S6 and S7). In this case some of the molecules (marked 11–13) showed different amounts of emission amplification every medium, thereby making their selective sensing impossible. All the molecules showing any selective emission enhancement contain a phenolic OH group, which can be essential in processes that manipulate the

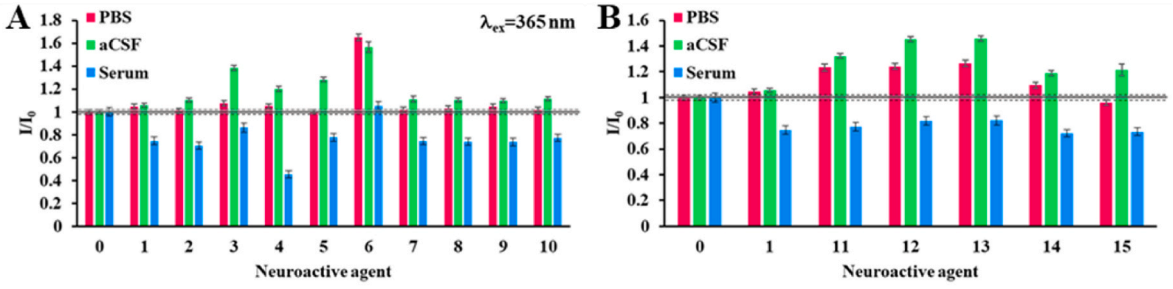

Fig. 7. Emission enhancement (I/I_0) of kynurenine (**A**) and serotonin (**B**) pathway molecules with identical concentrations (34.4 μM) in PBS, aCSF and diluted human serum (c_{metal} = 7.78 μM).

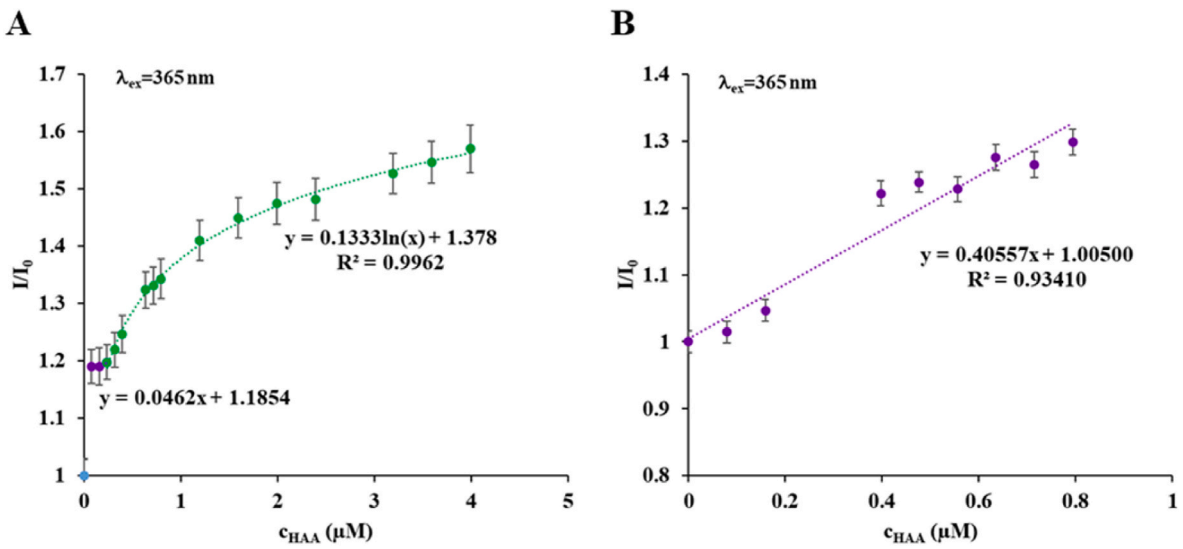

Fig. 8. Limit of detection (LOD) calculations of 3-HAA in PBS (**A**) and in aCSF (**B**) medium (c_{NCs} is 0.1x of clean stock).

fluorescence of the NCs. Although Kyna also possesses an OH group connected to an aromatic ring (4-hydroxyquinoline), it does not show any effect, meaning that this ligand cannot change the fluorescence. This might be because of the nitrogen atom present in the ring, which supports keto-enol tautomerism in the molecule, with the equilibrium largely shifted to the ketone form.

3.4. Evaluation of potential interaction between Tf and 3-HAA with ITC

To investigate the interaction of Tf-AuAg NCs and 3-HAA ligand, calorimetric measurements have been performed. This investigation was also extended to pure Tf protein in order to prove the role of the NCs as potential materials for sensing applications. The results are shown in Fig. 9. The ITC studies were performed according to the concentration conditions set during the fluorescence spectroscopy tests, focusing on the smaller molar ratio region. Based on the findings of the ITC tests, there is no detectable binding interaction between the 3-HAA and the pure Tf. The measurements were repeated with the bimetallic NCs stabilized by Tf, using the same protein concentration as in the first test. In this case we found that there is a selective binding between the reactants. Fitting the registered data with the one binding site model gives the thermodynamic parameters of the reaction. The molar free enthalpy is around −36 kJ mol^{-1} meaning the reaction is favored; molar enthalpy gives 13.1 kJ mol^{-1} for Tf-AuAg NCs, while molar entropy is 165 J mol^{-1} K^{-1}. Considering the relationship between ΔH and TΔS, we can see that the binding process is endothermic and entropy-driven. The n parameter representing the estimated number of binding sites (N) was 1.03 ± 0.01, while the binding constant (K_a) was 2.17 ± 0.33 × 10^6 M^{-1}. Taking these results into consideration, the change in the fluorescence property can be attributed to the structural modification resulting from the direct binding of the ligand to the protein. The FT-IR and CD studies presented above proved the structure-changing effect of NC formation, which suggests that new amino acids could appear on the surface of the NCs, forming possible binding regions for 3-HAA in Tf.

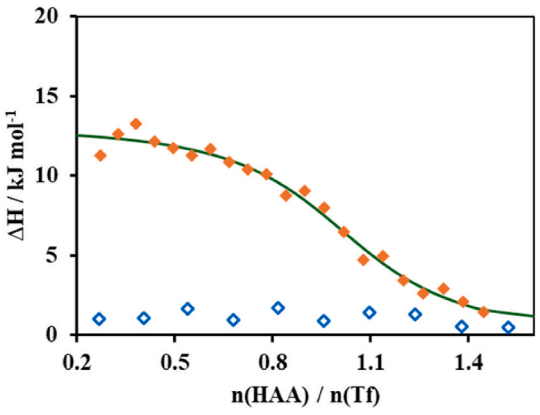

Fig. 9. Isotherm titration calorimetry of 3-HAA with Tf and Tf-AuAg NCs. Full symbols: enthalpograms of the interaction between the clusters and 3-HAA; empty symbols: enthalpograms from the protein and ligand interaction; solid green line: the fitted curve of the one-binding site model.

4. Conclusion

Summarizing our results, we successfully synthesized novel Tf-stabilized bimetallic AuAg NCs. The development of our preparation protocol has led to a four times better fluorescence intensity compared to single-metal systems, without the use of other reductants. We followed an optimization process based on five different synthesis parameters (metal ratio, Tf concentration, temperature, metal concentration, and synthesis time) to maximize inherent fluorescence. The resulting material underwent a cleaning process based on dialysis, and the sample was characterized and compared to free Tf and monometallic gold NCs. The properties of NCs were assessed, focusing on the Tf and the metal core, with greater interest in optical properties. Quantum yield measurements showed that the NCs perform as well as other protein-stabilized NCs, albeit they have lower values compared to some Tf-Au NCs presented in the literature. It must be mentioned that the values cannot be compared directly, because the determination methods for quantum yield were different (using rhodamine B versus a calibrated light source as reference). Fluorescence excitation and emission were thoroughly analyzed, separating individual peaks coming from metal- and ligand-based emissions. With the help of 3D fluorescence spectra, quenching studies using iodide ions and fluorescence lifetime measurements, we could divide the excitation and emission spectra into different peaks, assigning protein- and nanocluster-related fluorescence processes to exact emission maxima and lifetimes. Finally, the NCs were employed in the sensing of tryptophan metabolites, namely from the kynurenine and serotonin pathways. Further experiments were conducted on 3-hydroxyanthranilic acid, where the LOD value was determined both in PBS (0.55 μM) and aCSF medium (0.32 μM). Unlike usual sensing studies, 3-HAA amplified the fluorescence of the bimetallic NCs, which is in accordance with the behavior of Tf-Au

NCs [17]. Temperature-dependent measurements were not performed, as these only provide valuable data in the case of sensing through fluorescence quenching. Some of the serotonin metabolites also increased fluorescence, but their separate determination could be compromised due to their interference. Structural similarities between the molecules that showed any enhancement in fluorescence intensity imply that the presence of phenolic OH is essential, but its role is still under investigation. While it is true that the intrinsic fluorescence of 3-HAA could be used for simple determination, the separation from other fluorophores would be very difficult. The application of Tf-AuAg NCs as a sensing material is supported by their fluorescence in the red region, where very few interfering molecules emit, enabling measurements to be performed without much disruption. Finally, ITC studies revealed a binding reaction between 3-HAA and Tf-AuAg NCs, suggesting the formation of one binding site for the molecule, which is not present in pure Tf protein.

CRediT authorship contribution statement

Árpád Turcsányi: Writing – original draft, Investigation, Conceptualization, Visualization, Formal analysis, Writing – review & editing, Methodology, Data curation. **Ádám Juhász:** Methodology, Investigation, Visualization. **Edit Csapó:** Visualization, Data curation, Writing – review & editing, Supervision, Conceptualization, Writing – original draft, Funding acquisition.

Declaration of competing interest

The authors declare that they have no known competing financial interests or personal relationships that could have appeared to influence the work reported in this paper.

Acknowledgement

This research was funded by the Project no TKP2021-EGA-32 with the support provided by the Ministry of Culture and Innovation of Hungary from the National Research, Development and Innovation Fund, financed under the TKP2021-EGA funding scheme. Á. Turcsányi is grateful for the support of the University Research Scholarship Program (EKÖP-24-3-SZTE-597) funded by the Ministry of Culture and Innovation through the National Fund for Research, Development and Innovation. The publication was also funded by the University of Szeged Open Access Fund (FundRef, Grant No. 7803).

Appendix A. Supplementary data

Supplementary data to this article can be found online at https://doi.org/10.1016/j.mtchem.2025.102835.

Data availability

Data will be made available on request.

References

[1] R. Jin, C. Zeng, M. Zhou, Y. Chen, Atomically precise colloidal metal nanoclusters and nanoparticles: fundamentals and opportunities, Chem. Rev. 116 (2016) 10346–10413, https://doi.org/10.1021/acs.chemrev.5b00703.
[2] W. Hou, F. Xia, G. Alfranca, H. Yan, X. Zhi, Y. Liu, C. Peng, C. Zhang, J.M. de la Fuente, D. Cui, Nanoparticles for multi-modality cancer diagnosis: simple protocol for self-assembly of gold nanoclusters mediated by gadolinium ions, Biomaterials 120 (2017) 103–114, https://doi.org/10.1016/J.BIOMATERIALS.2016.12.027.
[3] T. Feng, Y. Chen, B. Feng, J. Yan, J. Di, Fluorescence red-shift of gold-silver nanoclusters upon interaction with cysteine and its application, Spectrochim. Acta Part A Mol. Biomol. Spectrosc. 206 (2019) 97–103, https://doi.org/10.1016/J.SAA.2018.07.087.
[4] H.N. Kagalwala, E. Gottlieb, G. Li, T. Li, R. Jin, S. Bernhard, Photocatalytic hydrogen generation system using a nickel-thiolate hexameric cluster, Inorg. Chem. 52 (2013) 9094–9101, https://doi.org/10.1021/ic4013069.
[5] L. Hu, Y. Yuan, L. Zhang, J. Zhao, S. Majeed, G. Xu, Copper nanoclusters as peroxidase mimetics and their applications to H2O2 and glucose detection, Anal. Chim. Acta 762 (2013) 83–86, https://doi.org/10.1016/J.ACA.2012.11.056.
[6] E. Khatun, T. Pradeep, New routes for multicomponent atomically precise metal nanoclusters, ACS Omega 6 (2021) 1–16, https://doi.org/10.1021/ACSOMEGA.0C04832.
[7] P.L. Xavier, K. Chaudhari, A. Baksi, T. Pradeep, Protein-protected luminescent noble metal quantum clusters: an emerging trend in atomic cluster nanoscience, Nano Rev. 3 (2012) 14767, https://doi.org/10.3402/NANO.V3I0.14767.
[8] J. Xie, Y. Zheng, J.Y. Ying, Protein-directed synthesis of highly fluorescent gold nanoclusters, J. Am. Chem. Soc. 131 (2009) 888–889, https://doi.org/10.1021/ja806804u.
[9] L. Chen, M. Gharib, Y. Zeng, S. Roy, C.K. Nandi, I. Chakraborty, Advances in bovine serum albumin-protected gold nanoclusters: from understanding the formation mechanisms to biological applications, Mater. Today Chem. 29 (2023) 101460, https://doi.org/10.1016/J.MTCHEM.2023.101460.
[10] R. Khandelia, S. Bhandari, U.N. Pan, S.S. Ghosh, A. Chattopadhyay, Gold nanocluster embedded albumin nanoparticles for two-photon imaging of cancer cells accompanying drug delivery, Small 11 (2015) 4075–4081, https://doi.org/10.1002/smll.201500216.
[11] A. Cantelli, G. Battistelli, G. Guidetti, J. Manzi, M. Di Giosia, M. Montalti, Luminescent gold nanoclusters as biocompatible probes for optical imaging and theranostics, Dyes Pigments 135 (2016) 64–79, https://doi.org/10.1016/J.DYEPIG.2016.06.019.
[12] A. Yahia-Ammar, D. Sierra, F. Mérola, N. Hildebrandt, X. Le Guével, Self-assembled gold nanoclusters for bright fluorescence imaging and enhanced drug delivery, ACS Nano 10 (2016) 2591–2599, https://doi.org/10.1021/acsnano.5b07596.
[13] F. He, X. Qin, L. Bu, Y. Fu, Y. Tan, C. Chen, Y. Li, Q. Xie, S. Yao, Study on the bioelectrochemistry of a horseradish peroxidase-gold nanoclusters bionanocomposite, J. Electroanal. Chem. 792 (2017) 39–45, https://doi.org/10.1016/J.JELECHEM.2017.03.033.
[14] S. Borse, Z.V.P. Murthy, T.J. Park, S.K. Kailasa, Lysozyme-decorated gold and molybdenum bimetallic nanoclusters for the selective detection of bilirubin as a jaundice biomarker, ACS Appl. Nano Mater. 4 (2021) 11949–11959, https://doi.org/10.1021/acsanm.1c02515.
[15] N. Zhang, Y. Si, Z. Sun, L. Chen, R. Li, Y. Qiao, H. Wang, Rapid, selective, and ultrasensitive fluorimetric analysis of mercury and copper levels in blood using bimetallic gold-silver nanoclusters with “silver effect”-enhanced red fluorescence, Anal. Chem. 86 (2014) 11714–11721, https://doi.org/10.1021/ac503102g.
[16] H. Chen, L. Lin, H. Li, J. Li, J.M. Lin, Aggregation-induced structure transition of protein-stabilized zinc/copper nanoclusters for amplified chemiluminescence, ACS Nano 9 (2015) 2173–2183, https://doi.org/10.1021/acsnano.5b00141.
[17] Q. Sha, B. Sun, C. Yi, R. Guan, J. Fei, Z. Hu, B. Liu, X. Liu, A fluorescence turn-on biosensor based on transferrin encapsulated gold nanoclusters for 5-hydroxytryptamine detection, Sensor. Actuator. B Chem. 294 (2019) 177–184, https://doi.org/10.1016/J.SNB.2019.05.060.
[18] X. Guo, M. Luo, D. Zhao, Y. Ge, Z. Yuan, S. Sang, X. Dong, A novel flexible magnetoelastic biosensor with “sandwich” structure based on transferrin encapsulated gold nanoclusters for 5-hydroxytryptamine detection, Microchem. J. 204 (2024) 111048, https://doi.org/10.1016/J.MICROC.2024.111048.
[19] L. Orsatti, T. Stiehl, K. Dischinger, R. Speziale, P. Di Pasquale, E. Monteagudo, C. Müller-Tidow, A. Radujkovic, P. Dreger, T. Luft, Kynurenine pathway activation and deviation to anthranilic and kynurenic acid in fibrosing chronic graft-versus-host disease, Cell Rep. Med. 2 (2021) 100409, https://doi.org/10.1016/J.XCRM.2021.100409.
[20] A.N. Kovács, N. Varga, Á. Juhász, E. Csapó, Serum protein-hyaluronic acid complex nanocarriers: structural characterisation and encapsulation possibilities, Carbohydr. Polym. 251 (2021) 117047, https://doi.org/10.1016/j.carbpol.2020.117047.
[21] V. Hornok, Á. Juhász, G. Paragi, A.N. Kovács, E. Csapó, Thermodynamic and kinetic insights into the interaction of kynurenic acid with human serum albumin: spectroscopic and calorimetric approaches, J. Mol. Liq. 313 (2020) 112869, https://doi.org/10.1016/J.MOLLIQ.2020.112869.
[22] V. Hornok, K.W.K. Amin, A.N. Kovács, Á. Juhász, G. Katona, G.T. Balogh, E. Csapó, Increased blood-brain barrier permeability of neuroprotective drug by colloidal serum albumin carriers, Colloids Surf. B Biointerfaces 220 (2022) 112935, https://doi.org/10.1016/J.COLSURFB.2022.112935.
[23] A. Ostapiuk, E.M. Urbanska, Kynurenic acid in neurodegenerative disorders—unique neuroprotection or double-edged sword? CNS Neurosci. Ther. 28 (2022) 19–35, https://doi.org/10.1111/CNS.13768.
[24] X. Le Guével, N. Daum, M. Schneider, Synthesis and characterization of human transferrin-stabilized gold nanoclusters, Nanotechnology 22 (2011) 275103, https://doi.org/10.1088/0957-4484/22/27/275103.
[25] D. Ungor, K. Horváth, I. Dékány, E. Csapó, Red-emitting gold nanoclusters for rapid fluorescence sensing of tryptophan metabolites, Sensor. Actuator. B Chem. 288 (2019) 728–733, https://doi.org/10.1016/j.snb.2019.03.026.
[26] D. Ungor, Á. Turcsányi, B. Torma, E. Csapó, Gold/silver bimetallic nanoclusters stabilized by immunoprotein: tuning the selectivity for identification of kynurenine pathway metabolites, J. Mol. Liq. 402 (2024) 124756, https://doi.org/10.1016/J.MOLLIQ.2024.124756.
[27] J.R. Lakowicz, Principles of Fluorescence Spectroscopy, Springer US, Boston, MA, 2006, https://doi.org/10.1007/978-0-387-46312-4.
[28] Á. Turcsányi, D. Ungor, M. Wojnicki, E. Csapó, Protein-stabilized bimetallic Au/Ag nanoclusters as fluorescent reporters: synthesis, characterization and their interactions with biocolloids, J. Mol. Liq. 370 (2023) 121002, https://doi.org/10.1016/J.MOLLIQ.2022.121002.

[29] H. Xie, Y. Wang, N. Zhang, S. Li, J. Li, X. Xin, Solvent-induced self-assembly of silver nanoclusters for white-light-emitting diodes and temperature sensing, ACS Appl. Nano Mater. 7 (2024) 1009–1018, https://doi.org/10.1021/acsanm.3c05006.
[30] Z. Xie, P. Sun, Z. Wang, H. Li, L. Yu, D. Sun, M. Chen, Y. Bi, X. Xin, J. Hao, Metal–organic gels from silver nanoclusters with aggregation-induced emission and fluorescence-to-phosphorescence switching, Angew. Chem. Int. Ed. 59 (2020) 9922–9927, https://doi.org/10.1002/ANIE.201912201.
[31] T.Q. Yang, B. Peng, B.Q. Shan, Y.X. Zong, J.G. Jiang, P. Wu, K. Zhang, Origin of the photoluminescence of metal nanoclusters: from metal-centered emission to ligand-centered emission, Nanomaterials 10 (2020), https://doi.org/10.3390/nano10020261.
[32] S. Wang, X. Meng, A. Das, T. Li, Y. Song, T. Cao, X. Zhu, M. Zhu, R. Jin, S. Wang, X. Meng, Y. Song, T. Cao, X. Zhu, M. Zhu, A. Das, R. Jin, T. Li, A 200-fold quantum yield boost in the photoluminescence of silver-doped AgxAu25−x nanoclusters: the 13 th silver atom matters, Angew. Chem. Int. Ed. 53 (2014) 2376–2380, https://doi.org/10.1002/ANIE.201307480.
[33] S.-S. Zhang, S. Havenridge, C. Zhang, Z. Wang, L. Feng, Z.-Y. Gao, C.M. Aikens, C.-H. Tung, D. Sun, Sulfide boosting near-unity photoluminescence quantum yield of silver nanocluster, J. Am. Chem. Soc. 144 (2022) 18305–18314, https://doi.org/10.1021/jacs.2c06093.
[34] C. Zhu, J. Xin, J. Li, H. Li, X. Kang, Y. Pei, M. Zhu, Fluorescence or phosphorescence? The metallic composition of the nanocluster kernel does matter, Angew. Chem. Int. Ed. 61 (2022) e202205947, https://doi.org/10.1002/anie.202205947.
[35] E. Goormaghtigh, J.M. Ruysschaert, V. Raussens, Evaluation of the information content in infrared spectra for protein secondary structure determination, Biophys. J. 90 (2006) 2946–2957, https://doi.org/10.1529/BIOPHYSJ.105.072017.
[36] S. Borse, Z.V.P. Murthy, S.K. Kailasa, Synthesis of gold and copper bimetallic nanoclusters with papain for fluorescence detection of cortisone in biological samples, Anal. Bioanal. Chem. 415 (2023) 335–343, https://doi.org/10.1007/s00216-022-04412-w.
[37] Y. Bi, Z. Wang, T. Liu, D. Sun, N. Godbert, H. Li, J. Hao, X. Xin, Supramolecular chirality from hierarchical self-assembly of atomically precise silver nanoclusters induced by secondary metal coordination, ACS Nano 15 (2021) 15910–15919, https://doi.org/10.1021/acsnano.1c03824.